Observations of Bedform Migration and Bedload Sediment Transport in Combined Wave-Current Flows

Wengrove, M. E.; Foster, D. L.; Lippmann, T. C.; de Schipper, M. A.; Calantoni, J.

DOI
10.1029/2018JC014555

Publication date
2019

Document Version
Final published version

Published in
Journal of Geophysical Research: Oceans

Citation (APA)
Wengrove, M. E., Foster, D. L., Lippmann, T. C., de Schipper, M. A., & Calantoni, J. (2019). Observations of Bedform Migration and Bedload Sediment Transport in Combined Wave-Current Flows. *Journal of Geophysical Research: Oceans*, *124*(7), 4572-4590. https://doi.org/10.1029/2018JC014555

JGR Oceans

RESEARCH ARTICLE
10.1029/2018JC014555

This article is a companion to Wengrove et al. (2018), https://doi.org/10.1029/2018JC014357.

Key Points:

- The total kinetic energy in the flow field and the bedform migration rate are directly proportional
- Sediment flux in combined wave currents was found to be greater than in wave dominant flows with comparable kinetic energy
- Data and comparison with bedload sediment flux models shows that energetics may be most representative of system physics

Supporting Information:

- Supporting Information S1

Correspondence to:
M. E. Wengrove,
meagan.wengrove@oregonstate.edu

Citation:
Wengrove, M. E., Foster, D. L., Lippmann, T. C., de Schipper, M. A., & Calantoni, J. (2019). Observations of bedform migration and bedload sediment transport in combined wave-current flows. *Journal of Geophysical Research: Oceans*, *124*. https://doi.org/10.1029/2018JC014555

Received 8 SEP 2018
Accepted 4 APR 2019
Accepted article online 3 MAY 2019

Observations of Bedform Migration and Bedload Sediment Transport in Combined Wave-Current Flows

M. E. Wengrove[1], **D. L. Foster**[2], **T. C. Lippmann**[3], **M. A. de Schipper**[4], **and J. Calantoni**[5]

[1]Civil and Construction Engineering, Oregon State University, Corvallis, OR, USA, [2]Mechanical Engineering and Ocean Engineering, University of New Hampshire, Durham, NH, USA, [3]Earth Sciences, University of New Hampshire, Durham, NH, USA, [4]Hydraulic Engineering, Delft University of Technology, Delft, Netherlands, [5]Marine Geoscience Division, U.S. Naval Research Laboratory, Washington, DC, USA

Abstract Bedload transport is an important mechanism for sediment flux in the nearshore. Yet few studies examine the relationship between bedform evolution and net sediment transport. Our work contributes concurrent observations of bedform mobility and bedload transport in response to wave dominant, current dominant, and combined wave-current flows in the nearshore. Bedload sediment flux from migrating bedforms during combined wave-current conditions accounted for at least 20% more bedload transport when compared with wave dominant flows and at least 80% more than current-dominant flows. Bedforms were observed to transport the most sediment during periods with strong currents, with high-energy skewed waves, and while bedform orientation and transport direction were aligned. Regardless of flow type, bedform migration rates were directly proportional to the total kinetic energy contained in the flow field. Eleven bedload transport models formulated to be used in combined flows (both shear and energetics based) were compared with sediment flux estimated from measured bedform migration. An energetics based sediment transport model was most representative for our data.

1. Introduction

Coastal morphodynamics is driven by sediment mobility in response to waves, currents, and combined wave-current flows. Sediment transport is broadly considered in two classifications, bedload and suspended load transport (van Rijn, 1993). Numerous studies have shown that the small-scale morphologic change is correlated to the bedload transport (Aagaard et al., 2001; Amos et al., 1999; Hay & Mudge, 2005; Soulsby & Damgaard, 2005). The focus of our effort was to examine the evolution of bedforms and by proxy bedload transport in combined wave-current environments during the intermediate energy states, where bedforms are mobile as they form, evolve, and migrate in response to waves, currents, or combined wave-current flows (Gallagher et al., 1998; Traykovski et al., 1999). Mobile bedforms are common in the surf zone, as well as in tidal inlets. Given that these regions only occasionally reach high-energy sheet flow transport conditions, it can be assumed that the intermediate energy states are important to understanding coastal morphodynamics.

Bedload transport via bedform migration can occur within mean wave, current, and combined wave-current flow conditions. In mean current-dominant flows, bedform migration occurs by grains being pushed up the stoss side of the bedform and deposited on the lee side (Fredsøe & Deigaard, 1992; van Rijn, 1993). In wave-dominant flows, migration of bedforms is thought to occur due to wave streaming and wave velocity skewness and/or wave velocity asymmetry (Davies & Villaret, 1999; Nielsen & Callaghan, 2003). In combined flows, transport typically is thought to occur by sediment being mobilized by waves and then advected by currents within the bottom boundary layer (Amos et al., 1999).

There are many observations of bedform response to wave-dominant or current-dominant flows (e.g., Nielsen, 1992; Soulsby et al., 2012; Traykovski et al., 1999; van Rijn, 1993); however, there are limited observations of bedform response to combined flows, especially in a field environment (Amos et al., 1999; Perillo et al., 2014; Smyth & Li, 2005; van Rijn, 2007). Existing data sets of bedform response to combined flows in the laboratory (e.g., Catano-Lopera & Garcia, 2006; Lacy et al., 2007; Perillo et al., 2014) and in the field (e.g., Amos et al., 1999; Gallagher et al., 1998; Passchier & Kleinhans, 2005; Soulsby et al., 2012; Sternberg, 1972) focus on bedform generation, roughness geometry, and orientation, but less frequently discuss bedload transport associated with the migration of combined flow bedforms. Additionally, the models that are developed to predict bedload transport within combined wave-current flows have not been widely compared to bedload sediment flux observations associated with bedform migration (Fredsøe et al., 1999; Grant & Madsen, 1979; Soulsby, 1997; Soulsby & Clarke, 2005; Soulsby & Damgaard, 2005; Sternberg, 1972; Styles & Glenn, 2000; van Rijn, 2007).

Our observations captured bedform evolution and migration in response to waves, currents, and combined wave-current flows at two cross-shore stations between the shore-parallel sandbar and the shoreline. Bedforms were exposed to storms and spring-neap tidal cycles, which generated a variety of flow conditions and transitions. The observed highly dynamic and nonequilibrium bedforms offer an opportunity to examine the response over a range of forcing conditions. Our effort addresses (1) bedform shape and mobility dependence on wave-dominant, current-dominant, and/or combined wave-current flows; (2) quantification of the sediment transport magnitude and direction associated with bedform evolution and migration within wave-dominant, current-dominant, and combined wave-current-dominant flows; and (3) the skill of existing models used to predict bedload transport in combined flows.

2. Methods

2.1. Experiment and Instrumentation

Data were collected during a field campaign at the Sand Engine meganourishment (the Netherlands) as part of MEGAPEX in the fall of 2014. Details of the experiment and instrumentation are described in Wengrove et al. (2018). There were two instrument stations: S1 located 20 m from the shoreline and S2 located 66 m further seaward along the same cross-shore transect and 50 m shoreward of the approximately shore parallel sandbar. At each station there was an Imagenex 881a pencil beam sonar with azimuth drive used to measure a complete topographic map of the local bedform shape and mobility, as well as an acoustic Doppler instrument to measure the local velocity field. Additionally, large-scale bathymetry was measured with regular surveys using an echo sounder and GPS mounted on a Jet Ski throughout the experiment. The coordinate system adopted herein is defined with respect to degrees from shore normal, with 0° being onshore ($-x$), +90° rotating counterclockwise from shore normal (toward the northeast, $+y$), and −90° rotating clockwise from shore normal (toward the southwest, $-y$). The sediment median grain size, d_{50}, was 350 μm.

2.2. Hydrodynamics

The local flow at each monitoring station was decomposed into current velocities, with magnitude U and direction ϕ_c, and wave orbital velocities, with magnitude u_o and direction ϕ_w, over 10-min-averaged time intervals; the current and wave components were used to estimate the combined wave current velocity and kinetic energy (Wengrove et al., 2018). The current velocity is defined by the resultant of the temporal mean of the horizontal (u, v) velocities with,

$$U = |\bar{u}|, \tag{1}$$

and the overbar represents a temporal average over 10 min. The magnitude of the representative orbital velocity assumes a sinusoidal velocity with,

$$u_o = \sqrt{2}u_{\mathrm{std}}, \tag{2}$$

where $u_{\mathrm{std}} = \overline{[(u - U)^2]}^{0.5}$ (Traykovski et al., 1999). The representative orbital velocity was used throughout the manuscript unless otherwise indicated by the bedload transport models evaluated in the discussion section.

The combined wave current velocity (Lacy et al., 2007) relates the wave orbital and current velocities with a third term representing the combined effect depending on the angle between the orbital and current velocities, where

$$u_{\mathrm{wc}} = [u_o^2 + U^2 + 2u_oU\cos|\phi_w - \phi_c|]^{0.5}. \tag{3}$$

Finally, the maximum kinetic energy in the combined wave-current flows is defined as

$$E_{k_{\mathrm{wc}}} = \frac{1}{2} u_{\mathrm{wc}}^2. \tag{4}$$

We distinguish between wave-dominant, current-dominant, and combined flow conditions using a fraction of energy approach to assess the contribution of waves and/or currents to sediment flux. An energy, $E_{k_{\mathrm{wc}}}$, approach is used instead of the friction velocity due to challenges in the friction velocity estimate in combined flow conditions over bedforms, so using energy mitigates propagation of error through analysis. $E_{k_w}/E_{k_{\mathrm{wc}}}$ is defined as the fraction of kinetic energy due to waves, so a value of 1 would be purely wave driven flow, and a value of 0 would be purely current driven flow. Previous literature has distinguished wave dominant flows from combined flows based on a ratio of wave-induced to current-induced friction velocity, where purely wave ripples occur at a friction velocity ratio of 0.5 or greater (Lacy et al., 2007; Sternberg, 1972). To put this limit in terms of energy, this threshold of 0.5 is squared. Therefore, we define, $E_{k_w}/E_{k_{\mathrm{wc}}} > 0.75$ to be wave dominant, $0.75 \geq E_{k_w}/E_{k_{\mathrm{wc}}} \geq 0.25$ for combined wave-current flow, and $0.25 > E_{k_w}/E_{k_{\mathrm{wc}}}$ to be current dominant. The nearbed velocity necessary for estimating the kinetic energy was taken at 10 cm above the bedform crests either by direct observation or approximation with linear wave theory for the wave contribution and a log layer approximation for the mean flow contribution (Mathisen & Madsen, 1996). The 10-cm distance was chosen because it is far enough away from the bedform crests to be minimally influenced by bedform vorticies, but close enough to the boundary to be representative of flow conditions near the bed. Further details of hydrodynamic calculations can be found in Wengrove et al. (2018) and Wengrove et al. (2017).

2.3. Bedform Migration and Sediment Flux

Aside from observations of bedform geometry, height (η), and wavelength (Λ; see Wengrove et al., 2018), a time series of bedform migration magnitude and direction was estimated using subsequent local 2-D bathymetric pairs from the pencil beam sonar. Each pair of bathymetries was processed with either a 2-D cross correlation as defined in Wengrove et al. (2017) or a motion estimator process least squares error approach (Perkovic et al., 2009). The 2-D cross correlation is a measure of similarity of the two bathymetries based on the displacement of one relative to the other, highlighting shifts (or bedform migrations) between bathymetries (similar to techniques used in Particle Image Velocimetry). If there are bedforms with multiple wavelengths within the sonar view window then the 2-D cross correlation method works well. However, when the bedforms get large, there may only be one wavelength in view; in this case, the motion estimator process method is a more robust method because the least squares analysis is much less sensitive for smaller viewing windows relative to bedform wavelength. Once the bedform displacement, $d_{xy} = (\boldsymbol{d}_x^2 + \boldsymbol{d}_y^2)^{0.5}$, was found between each subsequent bathymetric pair, the bedform migration rate and migration direction were found by $V_{\mathrm{mig.}} = d_{xy}/t_s$ and $\phi_{\mathrm{mig.}} = a\tan(\boldsymbol{d}_y/\boldsymbol{d}_x)$, respectively, where t_s is the sampling time between bathymetric pairs (Wengrove et al., 2017, 2018).

The transformation of bedform migration rate to volumetric bedload transport, q, has been characterized with magnitude,

$$q_{\mathrm{bedform}} = \frac{1}{2} n V_{\mathrm{mig}} \eta, \tag{5}$$

and direction (ϕ_{mig}), where n is the volume fraction of sediment and η is the bedform height (Amos et al., 1999; Traykovski et al., 1999). The formulation assumes that when the bedform migrates, the entire bedform is transported, and that the sand transport is equivalent to the trapezoid defined by the moving ripple face through time (Amos et al., 1999). The method described in (5) effectively yields the maximum bedform transport rate assuming a steady bedform volume between finite sampling measurements. Details of bedform statistics obtained from 2-D wavenumber spectra of the sonar imagery data including bedform wavelength (Λ), height (η), and orientation (ϕ_r) can be found in Wengrove et al. (2018) and Wengrove et al. (2017). Finally, bedform dimensionality (2-D/3-D) was determined from the bedform directional spread in the 2-D wavenumber spectra (Wengrove et al., 2018), where the delineation between 2-D and 3-D was defined with a spread of <20° for 2-D bedforms.

2.4. Prediction of Bedload Transport Magnitude

Since direct measurements of bedload transport are difficult and time consuming to obtain, it is generally inferred from the velocity field using measured and modeled data. There are two broad approaches to infer

Table 1
Bedload Transport Models

Model reference	Foundation	Formulation	Abbreviation
van Rijn et al. (2004)	$q_b = f(\tau_b)$	imbedded τ_b	VR04
van Rijn (2007)	$q_b = f(\tau_b)$	imbedded τ_b	VR07
Soulsby (Soulsby, 1997)	$q_b = f(\tau_b)$	imbedded τ_b	S97
van der A et al. (2013)	$q_{\mathrm{net}} = f(\tau_b)$	imbedded τ_{net}	VDA13
Meyer-Peter and Muller (1948) + Madsen (1994)	$q_b = f(\tau_b)$	explicit q_b+τ_b	MPM-M94
Meyer-Peter and Muller (1948) + Nielsen (1992) & Sternberg (1972)	$q_b = f(\tau_b)$	explicit q_b+τ_b	MPM-N92S72
Meyer-Peter and Muller (1948) + Soulsby and Clarke (2005)	$q_b = f(\tau_b)$	explicit q_b+τ_b	MPM-SC05
Meyer-Peter and Muller (1948) + Styles and Glenn (2000)	$q_b = f(\tau_b)$	explicit q_b+τ_b	MPM-SG00
Soulsby and Damgaard (2005) + Soulsby and Clarke (2005)	$q_b = f(\tau_b)$	explicit q_b+τ_b	SD05-SC05
Soulsby-van Rijn (Soulsby, 1997)	$q_b = f(u^n)$	energetics	SVR97
Hsu et al. (2006)	$q_b = f(u^n)$	energetics	HEG06

sediment flux from velocity measurements. The first assumes that $q_b = f(\tau_b \text{ or } \theta)$, indicating that bedload flux is a function of dimensional or nondimensional bed stress (Shields, 1936), and the second assumes that $q_b = f(u^n)$, a family of equations referred to as energetics models (Bagnold, 1966; Bailard & Inman, 1981; Bowen, 1980). Table 1 lists 11 models that are commonly used to estimate bedload sediment transport within the nearshore. Table 1 also includes a model foundation, which indicates whether the model is based in shear stress or energy. Within the shear stress based models, the various formulations are characterized as either explicit or imbedded, where the explicit models require an outside measurement or approximation of bed stress, and the imbedded models have a shear stress model imbedded in the transport formulation. The remainder of this section introduces each family of transport models and provides insight into where each is currently being implemented. Additionally, the supplementary information to this manuscript guides readers through the basis of the physics included in each model, for additional information and for the model formulations, references to each model are included in Table 1 and in the supporting information.

Within the stress-based family of transport models that assumes $q_b = f(\tau_b \text{ or } \theta)$, there are many explicit semiempirical models for bedload transport that require an external bed stress measurement or formulation (Soulsby, 1997). The shear stress family of models is widely used within field and laboratory data analysis because direct measurements of bed shear inferred from boundary layer gradients can be used within these models. The most common of these explicit semiempirical models is the excess stress based Meyer-Peter and Muller (1948) model. Excess stress based models characteristically subtract the critical threshold of motion nondimensional shear stress, θ_{crit}, from the flow Shields parameter, θ, but have varying gain factors and power exponents (Nielsen, 1992; Soulsby, 1997). The Meyer-Peter Muller model is shown to estimate bedload flux well when there is reasonable confidence in estimates of bed stress (Rodriguez-Abudo & Foster, 2014). If direct stress measurements are unavailable, these transport models can be paired with external formulations to estimate bed stress or to estimate θ. Common formulations to estimate the bed stress in combined flows include Styles and Glenn (2000), Madsen (1994), Soulsby and Clarke (2005), and Nielsen (1992) combined with Sternberg (1972). The bed stress in all of these models is estimated using current and wave friction factors. Meyer-Peter and Muller (1948) and derivatives are used widely with various bed stress approximations to estimate bedload transport. Soulsby and Damgaard (2005) is an example of another excess stress based transport model that is specifically formulated for use in combined wave-current flows incorporating the Soulsby and Clarke (2005) bed stress approximation.

The imbedded style of transport models still assume $q_b = f(\tau_b \text{ or } \theta)$ but have an imbedded stress model using friction factors. Models that are formulated in this manner include van Rijn (1993), van Rijn et al. (2004), van Rijn (2007), Soulsby (Soulsby, 1997), and van der A et al. (2013). Each of these models, excluding the van der A et al. (2013), assumes that intrawave dynamics are steady, while van der A et al. (2013) is a semiunsteady transport model.

Finally, the energetics family of transport models assume that the sediment flux is a function of the imposed free stream flow field, or $q_b = f(u^n)$ (Bagnold, 1966; Bailard & Inman, 1981; Bowen, 1980). Unlike an excess stress model, the energetics models directly relate bedload transport to higher moments of the velocity field including skewness and asymmetry. Hsu et al. (2006) modified the energetics models from Bagnold (1966), Bowen (1980), and Bailard and Inman (1981) to include transport from both waves and currents over a sandbar. Soulsby/van Rijn is another energetics-based model based upon the flow turbulent kinetic energy over a rippled sediment bed (Soulsby, 1997). Energetics based models generally have a drag coefficient based upon the boundary roughness as well as an efficiency parameter that approximates the magnitude of flow kinetic energy driving boundary mobility.

Large-scale coastal change models such as Delft3D (Lesser et al., 2004), XBeach (Roelvink et al., 2015), and COAWST (Warner et al., 2008) implement stress-based sediment transport models. The van Rijn (1993), van Rijn et al. (2004), van Rijn (2007), and van der A et al. (2013) approaches are used in Delft3D, XBeach implements the Soulsby/van Rijn (Soulsby, 1997) formulation, while COAWST uses the Meyer-Peter and Muller (1948) transport model with Styles and Glenn (2000) bed stress approximation or Soulsby and Damgaard (2005) transport model with Soulsby and Clarke (2005) bed stress approximation. While energetics-based models are often used to estimate cross-shore sediment transport, specifically related to sandbar evolution, but are not widely used to estimate bedload transport in processed based coastal change models. Our contribution compares each sediment transport model to observations of bedform migration.

2.5. Prediction of Bedload Transport Direction

When bedforms migrate, they transport their mass in a direction oriented in someway to the prevailing flow direction. The maximum gross bedform normal transport (MGBNT) is a method to estimate the bedform migration direction from the direction of the flow field, a quantity that does not distinguish wave and current directions (Gallagher et al., 1998; Lacy et al., 2007). The MGBNT is defined by the combined influence of the transport directions over the timescale of the bedform development; bedforms align to maximize their gross normal transport. The MGBNT occurs at an angle, α, in which the transport T is maximized.

$$\boldsymbol{T} = \sum_i D_i |\sin(\gamma_i - \alpha)| \tag{6}$$

where D_i and γ_i are the magnitude and direction of individual transport vectors (Gallagher et al., 1998). The summation window is dependent on the timescale of the bedform development/adjustment.

3. Results

3.1. Flow Forcing Bedform Shape and Migration

Observations obtained during MEGAPEX captured bedform response to wave, current, and combined wave-current flow conditions. Both ripples and megaripples were observed at S1 and S2 during the 2014 deployment (Wengrove et al., 2018). Time series of bedform variability in dimensionality, size, and migration rate with concomitant flow energy magnitude and dominance at site S1 is shown in Figure 1. Confidence limits in observed bedform wavelength was determined by the spread in the energy density peak in the 2-D wavenumber spectra (Wengrove et al., 2018) and are shown in representative snapshots from the S1 time series of wave, current, and combined flow dominant bedform evolution (Figures 2–5). At times bedforms were 2-D or 3-D (commonly occurring during periods of flow transitions) and were observed during current-dominant, wave-dominant, and combined wave-current energy conditions (Figures 1c and 1d). Megaripples were observed during periods with higher flow energy, and during energetic combined wave-current flow and lunate megaripples were observed on three occasions at S1 (Figures 1c and 1d, highlighted in blue). In addition to bedform shape and orientation, migration rate and migration direction also shift in response to flow forcing within current-dominant (Figure 2), wave-dominant (Figure 3), and combined wave-current flow conditions (Figures 4 and 5).

As flow conditions approached current dominance, the transition from wave to current dominance was gradual (e.g., with the onset of flood tidal flow). During the transition, the bedform transport direction led the bedform orientation (as shown in Figures 2a and 2e–2j) by approximately 40 min to 1 hr, which is also approximately equal to one third of the bedform growth adjustment time, τ (Wengrove et al., 2018).

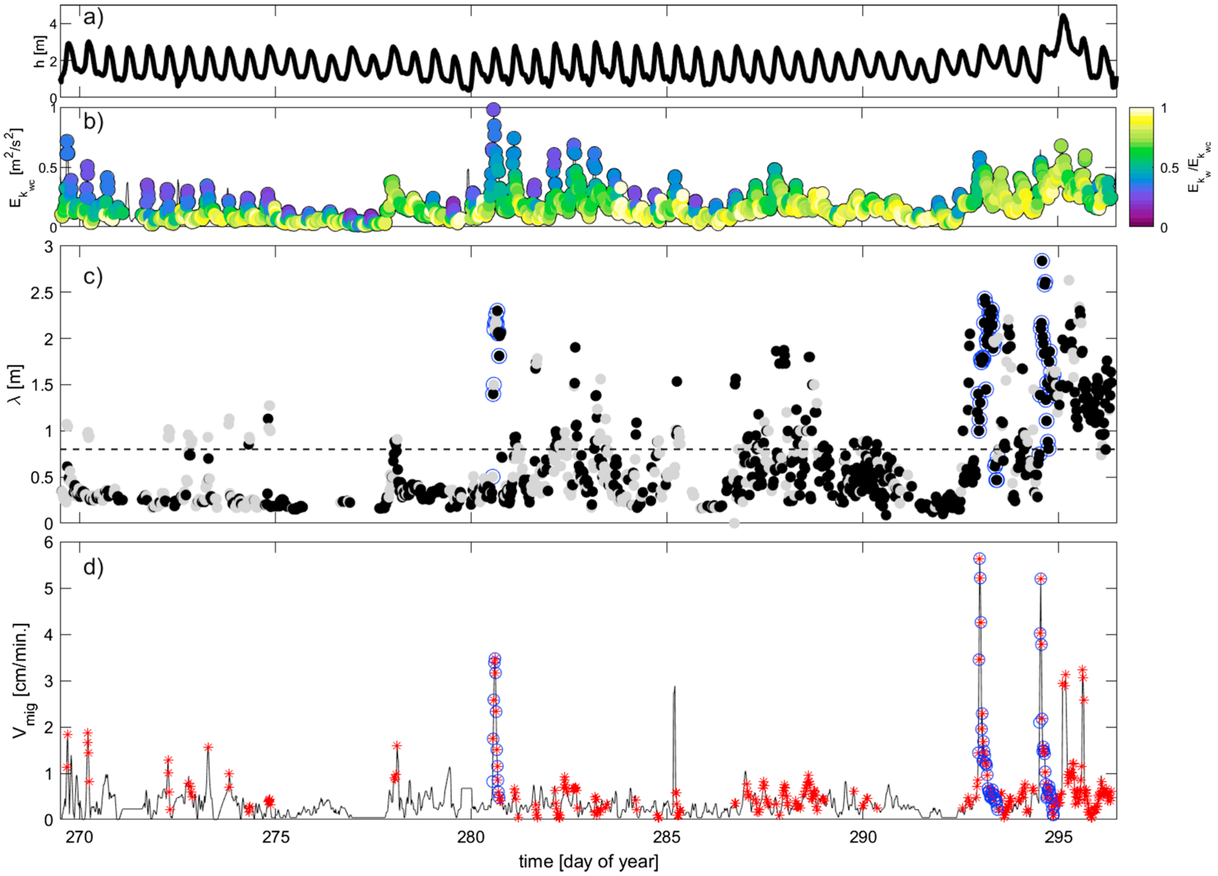

Figure 1. Time series showing bedform dimensionality (2-D/3-D) and scale (ripple/megaripple) in response to flow energy at S1. Panel (a) shows the depth, h, over the 30-day observational window. Panel (b) shows the total kinetic energy, $E_{k_{wc}}$ colored by fraction of kinetic energy due to waves $E_{k_w}/E_{k_{wc}}$. Panel (c) shows bedform wavelength, Λ, colored by the bedform dimensionality, 2-D bedforms are in gray and 3-D bedforms are in black. Bedforms with wavelengths greater than the dashed line are considered to be megaripples, with points highlighted with blue o showing observed occurrences of lunate megaripples. Panel (d) shows the bedform migration rate, $V_{mig.}$ (solid black line), with red * indicating occurrences of megaripples, and blue o showing observed occurrences of lunate megaripples.

The bedform adjustment time is defined as the time between zero crossings of $\mathrm{d}\Lambda/\mathrm{d}t$, where Λ is the bedform volume. Additionally, the migration velocity began to ramp up before the bedform wavelength evolved (Figure 2c) to the longer and fairly small steepness ($\eta/\Lambda = 0.06$) bedform shown in Figures 2g–2j). Such bedforms have a steepness consistent with dunes as observed by Fredsøe and Deigaard (1992). Observations of transport with a phase lead between migration direction and bedform orientation occurred frequently during the onset of spring flood tide at both sites S1 and S2.

Wave-dominant flow occurred during typical conditions (no storm), as well as during swell conditions (just before a storm; Figure 1). Bedforms were classified as wave-orbital ripples, with wavelength and height dependent on the energy in the flow field (Wengrove et al., 2018). Wave-dominant bedforms were usually 2-D in shape, as seen with the small spread in bedform direction (Figures 3d and 3e–3j). Bedforms migrated farther when the ripple orientation and migration direction were aligned (Figures 3h-3j compared with panel c).

During periods of combined wave-current flow there were several instances of megaripples with wavelengths of >0.8 m (Aagaard et al., 2001; Gallagher et al., 1998; Ngusaru & Hay, 2004) and migration rates in excess of 2 cm/min. Megaripples generally transitioned from 3-D to 2-D over the course of their evolution. Figure 4 shows the evolution of a representative megaripple during combined wave current flows at S1 (other instances of megaripples are highlighted in Figure 1c). When the combined flows become fairly strong, with total kinetic energy levels of greater than 0.5 m^2/s^2, lunate megaripples are observed migrating through the field of view (Figures 5f–5h; at S1 occurring on three occasions). Previously observed lunate megaripples in the nearshore by Ngusaru and Hay (2004) and Hay and Mudge (2005) generally occur under

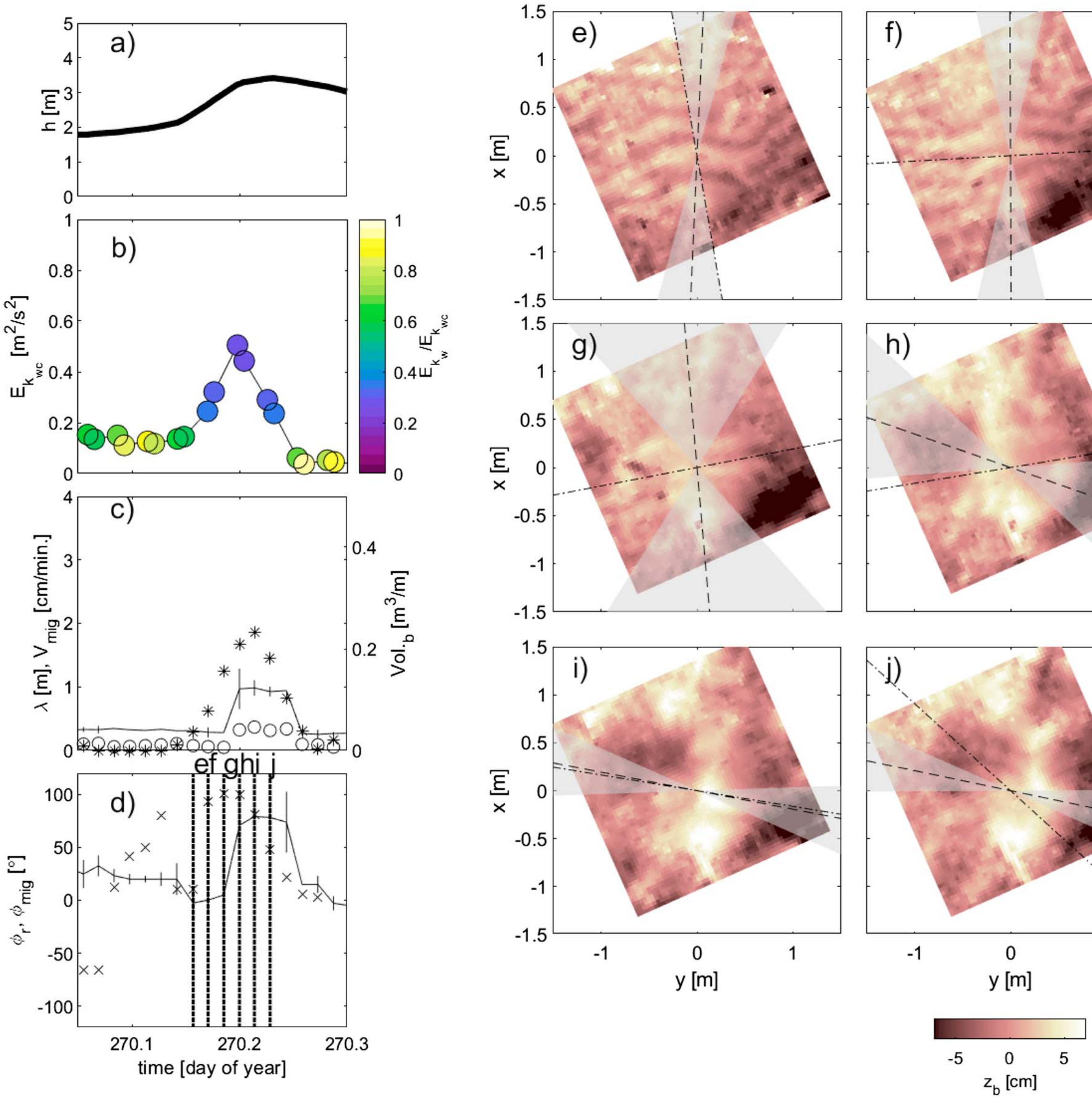

Figure 2. Time series of bedform adjustment with the onset of a flood tidal current at S1. Panel (a) shows the depth, h. Panel (b) shows the total kinetic energy, $E_{k_{wc}}$ colored by fraction of kinetic energy due to waves $E_{k_w}/E_{k_{wc}}$. Panel (c) shows the bedform migration rate, $V_{\text{mig.}}$ (*), corresponding bedform wavelength Λ (solid black line with vertical range bars representing wavelength uncertainty) (left axis), and bedform volume, Λ_b (o; right axis). Panel (d) shows the bedform orientation, ϕ_r (solid black line with vertical range bars representing directional spread), and bedform migration direction, $\phi_{\text{mig.}}$ (×). Panels (e)–(j) show sample local bathymetries taken at times indicated by the vertical dotted lines in (d), where the dashed line and shaded region in each panel indicate the bedform orientation (ϕ_r) and directional spread, respectively, and the dash-dotted line indicates the bedform migration direction ($\phi_{\text{mig.}}$).

weak mean currents and observe the horns of the lunate bedform migrating in the onshore direction. However, Thornton et al. (1998) qualitatively observed lunate megaripples migrating in the alongshore direction; an observation that is consistent with our observations where the horns of the bedform were migrating in the alongshore direction. Near the tip of the Sand Engine at S1, we observed lunate megaripples migrating toward the northeast, in the prevailing direction of the flood tidal current. The migration of the bedform preceded the growth of the bedform wavelength (Figure 5b), and the building period was shorter with higher energy flows.

Boxplot diagrams quantify the contributions to bedload transport driven by wave-dominant, current-dominant, and combined wave-current flows (Figure 6). Figure 6 shows several boxplots of relevant variables (bedform volume, bedform height, and bedform migration rate) to calculate sediment flux, as well as boxplots that present the sediment flux distributions at both S1 and S2. A boxplot is a simple

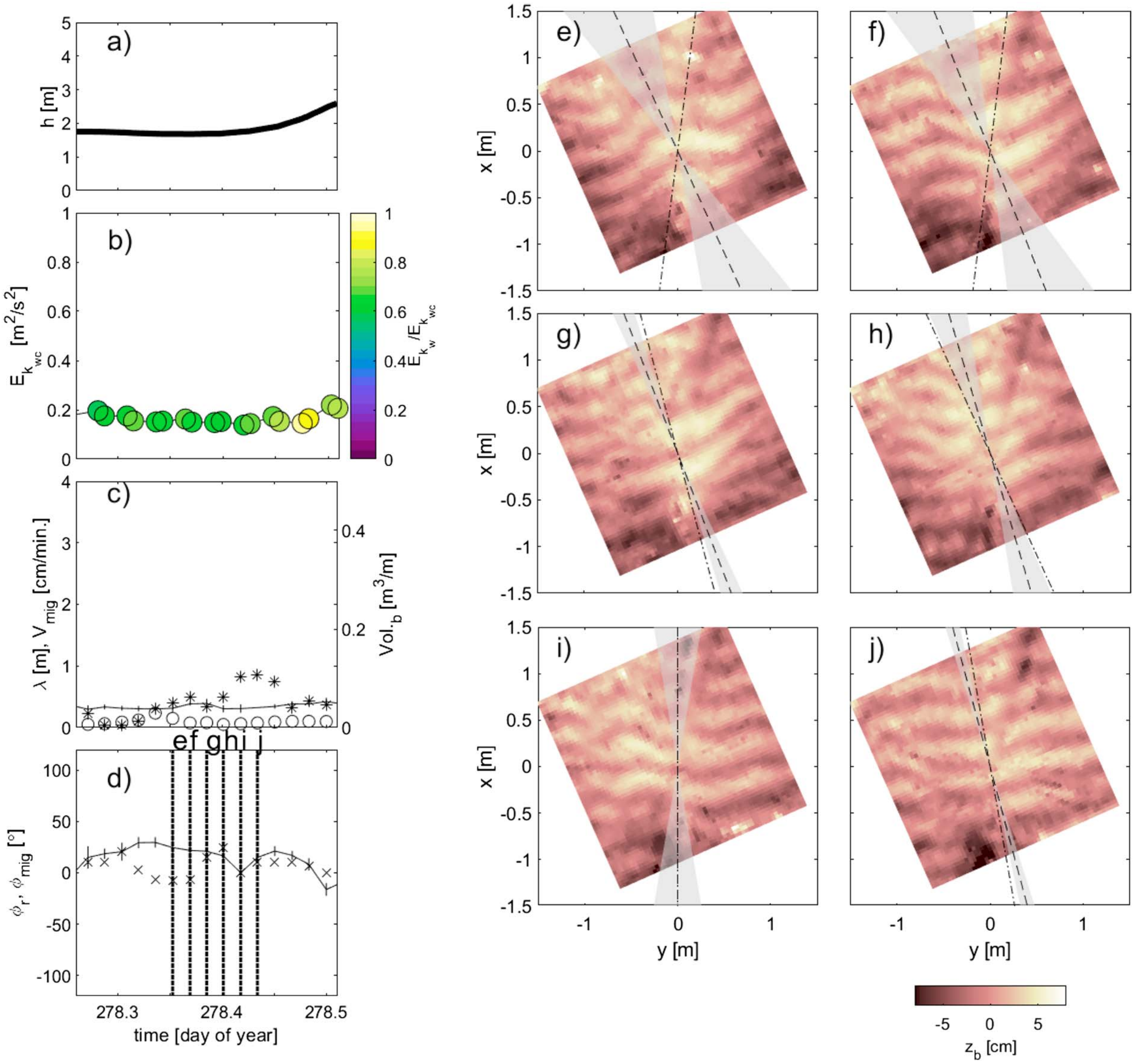

Figure 3. Time series of bedform adjustment in wave dominant flow at S1. Panel (a) shows the depth, h. Panel (b) shows the total kinetic energy, $E_{k_{wc}}$ colored by fraction of kinetic energy due to waves $E_{k_w}/E_{k_{wc}}$. Panel (c) shows the bedform migration rate, $V_{mig.}$ ($*$), corresponding bedform wavelength Λ (solid black line with vertical range bars representing wavelength uncertainty) (left axis), and bedform volume, Λ_b (o; right axis). Panel (d) shows the bedform orientation, ϕ_r (solid black line with vertical range bars representing directional spread), and bedform migration direction, $\phi_{mig.}$ (×). Panels (e)–(j) show sample local bathymetries taken at times indicated by the vertical dotted lines in (d), where the dashed line and shaded region in each panel indicate the bedform orientation (ϕ_r) and directional spread, respectively, and the dash-dotted line indicates the bedform migration direction ($\phi_{mig.}$).

way to represent the distribution of data. The distribution mean (MN) and median (MD) are used as distinguishing statistics between flow conditions. Additionally, for reference, a histogram of the occurrences of wave-dominant, current-dominant, and combined wave-current flows both at S1 and S2 are shown in Figures 6a and 6b.

On average, at both sites, the median transport in combined flows was $0.2\ \text{m}^3/\text{m/s}$, which was 15% and 91% larger than wave-dominant and mean current-dominant flow, respectively. Furthermore, on average the mean transport was $0.38\ \text{m}^3/\text{m/s}$ in combined flows, which was 24% and 82% greater than wave-dominant and mean current-dominant flow, respectively. Bedform behavior at site S1 (closer to shore) was more heavily influenced by combined flows, where mean combined flow transport accounted for a 45% greater sediment flux than wave dominant transport. At S2, the transport was comparable between wave dominant and combined wave-current flows (note that S2 was not deployed during the larger storm events). Boxplot diagrams for S1 show distributions of the full 27-day deployment, whereas boxplot diagrams for S2 only

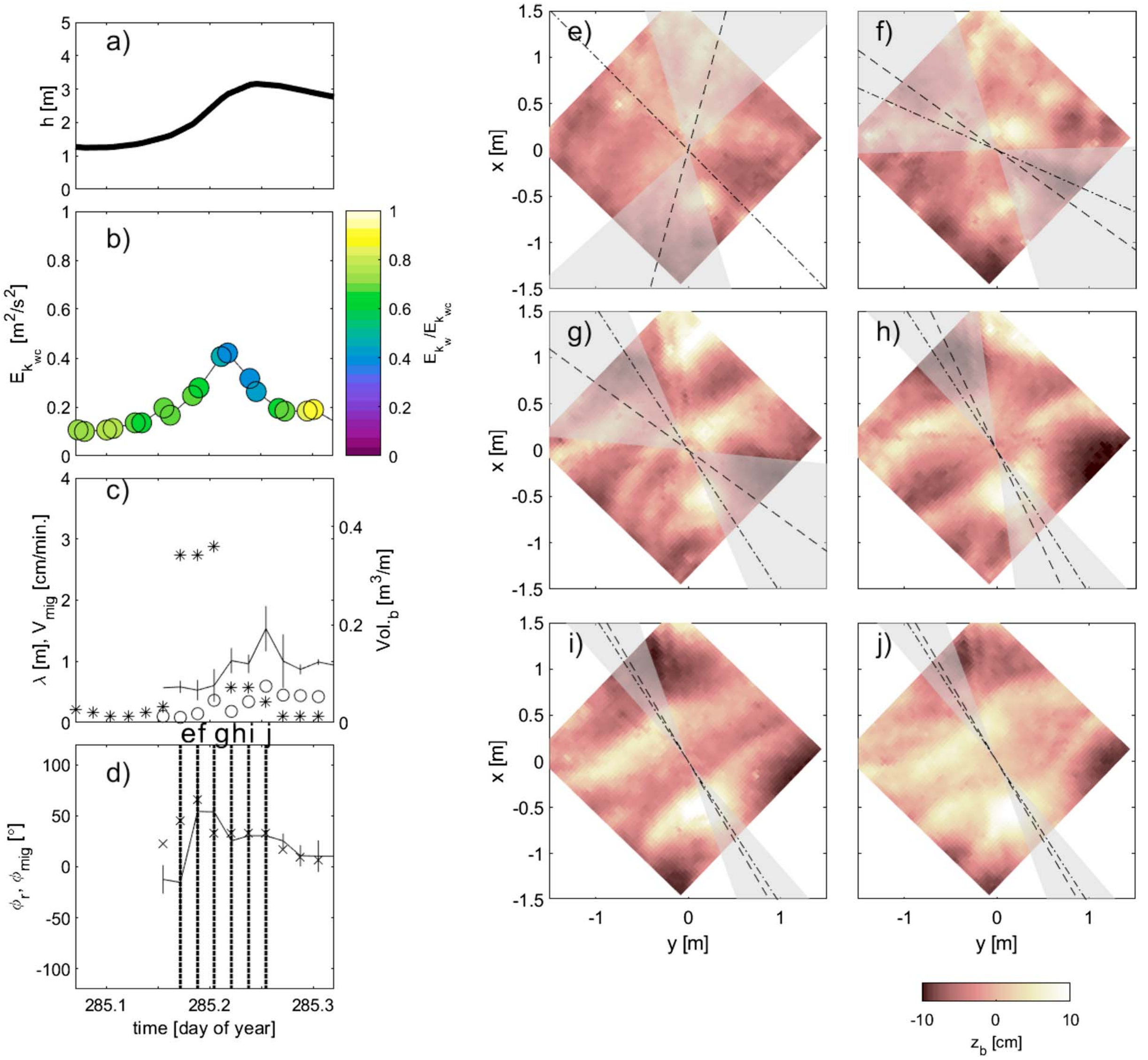

Figure 4. Time series of bedform adjustment during combined flow at S1—megaripple evolution. Panel (a) shows the depth, h. Panel (b) shows the total kinetic energy, $E_{k_{wc}}$, colored by fraction of kinetic energy due to waves $E_{k_w}/E_{k_{wc}}$. Panel (c) shows the bedform migration rate, $V_{\mathrm{mig.}}$ ($*$), corresponding bedform wavelength Λ (solid black line with vertical range bars representing wavelength uncertainty; left axis), and bedform volume, Λ_b (o; right axis). Panel (d) shows the bedform orientation, ϕ_r (solid black line with vertical range bars representing directional spread), and bedform migration direction, $\phi_{\mathrm{mig.}}$ (×). Panels (e)–(j) show sample local bathymetries taken at times indicated by the vertical dotted lines in (d), where the dashed line and shaded region in each panel indicate the bedform orientation (ϕ_r) and directional spread, respectively, and the dash-dotted line indicates the bedform migration direction ($\phi_{\mathrm{mig.}}$).

represent the middle 16 days; distributions for only the middle 16 days at S1 show similar trends to the S2 distributions (not shown). Transport contributions from combined flows were up to 50% greater than sediment flux associated with wave dominant flows, and even more so with current-dominant flows (Figure 6f).

3.2. Observations of Bedform Migration Direction

The observed bedform migration direction relative to the current and wave directions for all data at S1 and S2 is shown in Figure 7. Bedform migration directions spanned from −50° to +100° from shore normal, with larger bedforms more commonly propagating to the northeast (toward the +90° direction) when the current was roughly +80° from shore normal. Using circular statistics, it is clear from the scatter that the orientation did not solely depend on the currents ($r^2 = 0.40$, rmse/$\sigma = 56°$) nor the waves ($r^2 = 0.20$, rmse/$\sigma = 37°$). Bedforms appear to migrate in response to some combination of the current and wave directions, resulting in a migration direction between ϕ_c and ϕ_w as shown by the MGBNT (Figure 7c).

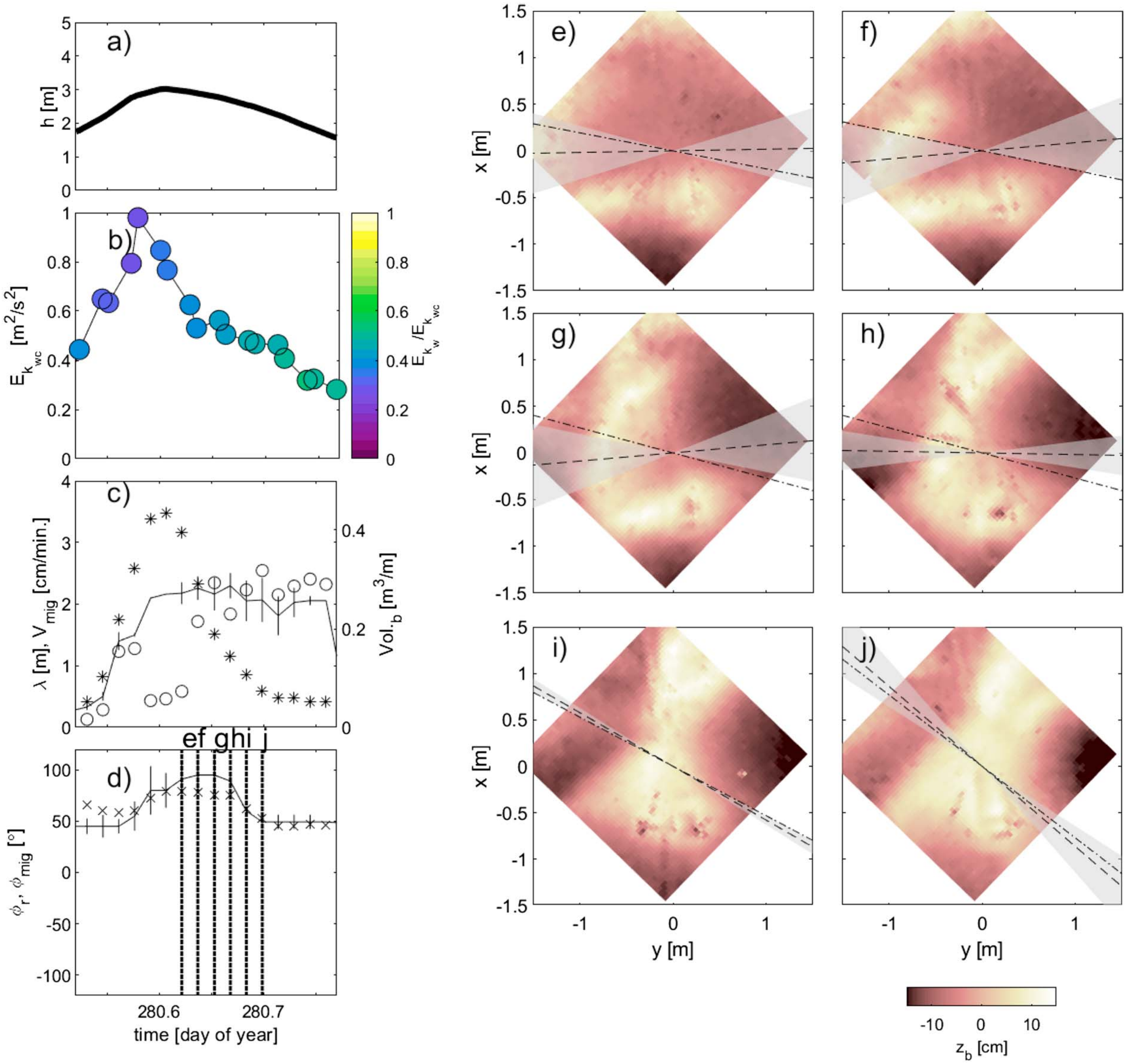

Figure 5. Time series of bedform adjustment during high energy combined flow at S1—lunate megaripple evolution. Panel (a) shows the depth, h. Panel (b) shows the total kinetic energy, $E_{k_{wc}}$, colored by fraction of kinetic energy due to waves $E_{k_w}/E_{k_{wc}}$. Panel (c) shows the bedform migration rate, $V_{\mathrm{mig.}}$ (*), corresponding bedform wavelength Λ (solid black line with vertical range bars representing wavelength uncertainty; left axis), and bedform volume, Λ_b (o; right axis). Panel (d) shows the bedform orientation, ϕ_r (solid black line with vertical range bars representing directional spread), and bedform migration direction, $\phi_{\mathrm{mig.}}$ (×). Panels (e)–(j) show sample local bathymetries taken at times indicated by the vertical dotted lines in (d), where the dashed line and shaded region in each panel indicate the bedform orientation (ϕ_r) and directional spread, respectively, and the dash-dotted line indicates the bedform migration direction ($\phi_{\mathrm{mig.}}$).

4. Discussion

4.1. Statistics of Bedform Migration and Implications for Transport

Bedform migration rates under wave, current, and combined wave-current flow in combination with the bedform shape characterize the bedload transport due to bedform migration. The bedform migration rate and height were used to estimate the bedload sediment flux due to moving bedforms with (5). There are several theories regarding the forcing mechanism for bedform migration, with mean currents and asymmetric velocities being the most prevalent (Davies & Villaret, 1999; Fredsøe & Deigaard, 1992; Nielsen & Callaghan, 2003; van Rijn, 1993). Five characteristic indicators of the flow field (current magnitude, orbital velocity magnitude, velocity skewness, velocity asymmetry, and total kinetic energy) are compared with bedform sediment flux for current-dominant (Figures 9a–9e), wave-dominant (Figures 9f–9j), and combined wave-current flows (Figures 9k–9o).

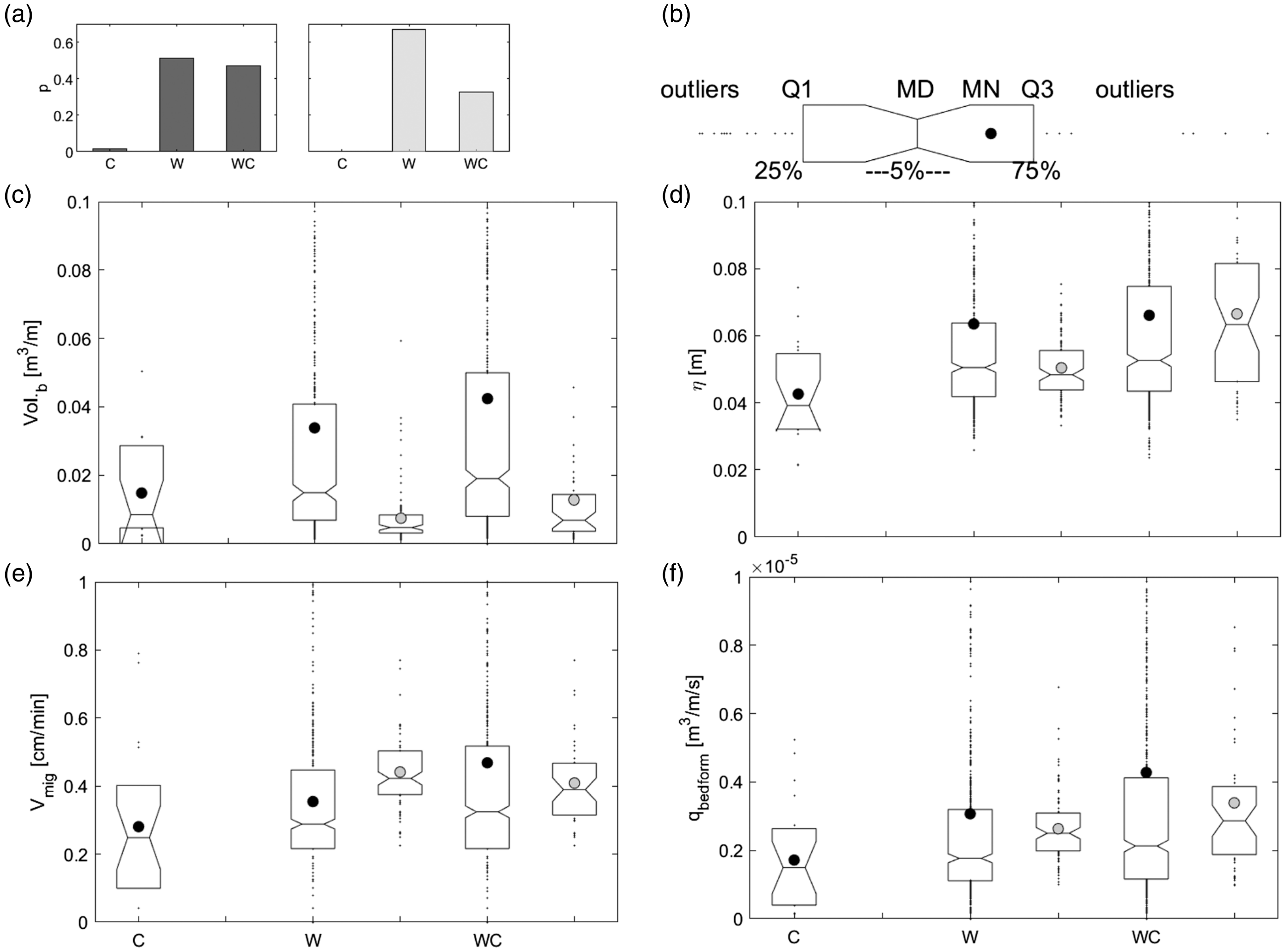

Figure 6. Boxplot diagrams showing relevant metrics for calculating sediment flux from bedform migration for current-dominant (C), wave-dominant (W), and combined wave-current (WC) flows. Panels (a) and (b) show the probability distributions of data falling into C/W/WC dominant flows for S1 and S2. Panel (c) shows boxplot diagrams of bedform volume, $\forall_b$. Panel (d) shows boxplot diagrams of bedform height, η. Panel (e) shows boxplot diagrams of bedform migration rate, V_{mig}. Panel (f) shows boxplot diagrams of bedform sediment flux, q_b. The mean point (MN) for site S1 is in black and site S2 is in gray on each boxplot. The key in the upper right hand corner of the figure shows relevant information for understanding a boxplot diagram. A boxplot is a simplistic method to represent a probability distribution. Q1 is the first quartile and contains 25% of the data, MD is the data median (shown by the center line), MN is the data mean (shown by the dot), and Q3 is the third quartile and contains another 25% of the data. The notch in the middle of the boxplot indicates the 95% confidence interval (shown by –5%– in the key), if the notch of one boxplot does not overlap with the notch of another, then the medians of the boxplots are statistically different with 95% confidence. The points to either side of Q1 and Q3 are outliers; note that all panels do not show the extent of their outliers so that the boxplot distribution is easier to distinguish.

All bedforms within current-dominant flows transported less than 0.1 $\times 10^{-4}$ m^3/m/s of sediment due to bedform migration with flow total kinetic energies up to 0.35 m^2/s^2 (Figure 9a), suggesting that current-dominant flows in our data set were not consistent with large sediment flux. Within current-dominant flows, there was not a strong relationship between sediment flux and orbital velocity, skewness, or asymmetry (Figures 9b–9d); however, the current-dominant bedforms did transport more sediment with increased flow energy (Figure 9e).

During wave dominant flows there were occurrences of sediment flux above 0.20×10^{-4} m^3/m/s (Figures 9f–9j) that occurred when the orbital velocity was large and the total kinetic energy was above 0.25 m^2/s^2 and also with increased velocity skewness (Figure 9h). Data show that in order for wave dominant bedforms to transport sediment at rates over 0.20 $\times 10^{-4}$ m^3/m/s, the waves not only must be skewed but also have a total kinetic energy over 0.4 m^2/s^2, there were only six observations of high energy skewed waves during the experiment (Figure 9h). Bedload sediment flux due to bedform migration was not shown

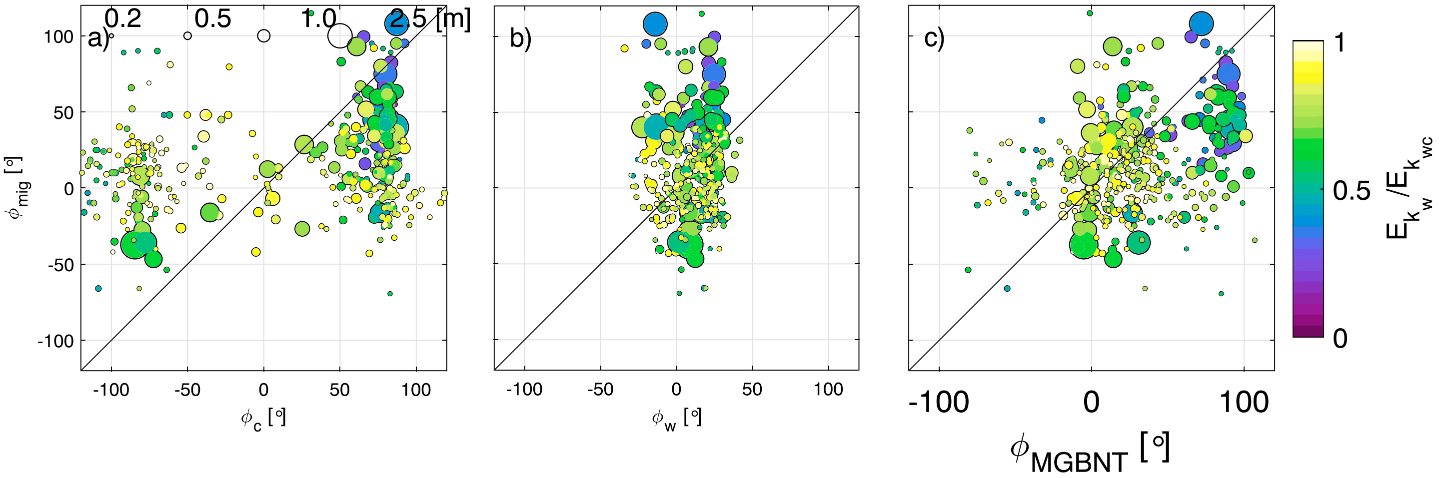

Figure 7. Scatter plots of bedform migration direction, $\phi_{\text{mig.}}$ (y axis) plotted against (a) the current direction, ϕ_c, (b) the wave direction, ϕ_w, and (c) the MGBNT direction, ϕ_{MGBNT} using a variable adjustment time τ (see section 4). Points are colored by fraction of energy due to waves and scaled by bedform wavelength, Λ, as indicated in (a). A 1:1 ratio line is plotted in black on each panel. MGBNT = maximum gross bedform normal transport.

to be related to velocity asymmetry (Figure 9i). One possible explanation is that velocity skewness leads to migration and velocity asymmetry contributes to fluidization (Foster et al., 2006; Sleath, 1999).

Finally, during combined flow conditions (Figures 9k–9o), periods of bedload sediment flux due to bedform migration greater than 0.20×10^{-4} m^3/m/s occurred when the current velocity magnitude increased above 0.5 m/s and the orbital velocity was larger than 0.5 m/s. During these events waves were sometimes (but not necessarily) skewed, and velocity asymmetry was low. In general, the observations indicate that for bedforms to migrate there needs to be either a strong current with a strong orbital velocity or skewed waves with a strong orbital velocity. Total kinetic energy in the flow field is an overarching indicator for increased bedform migration rates and bedload sediment flux due to bedform migration regardless of whether the flow is wave, current, or combined wave-current dominant.

The bedform migration rate and sediment flux were shown to increase with increased total kinetic energy, regardless of whether conditions were wave-dominant, current-dominant, or combined wave-current flows,

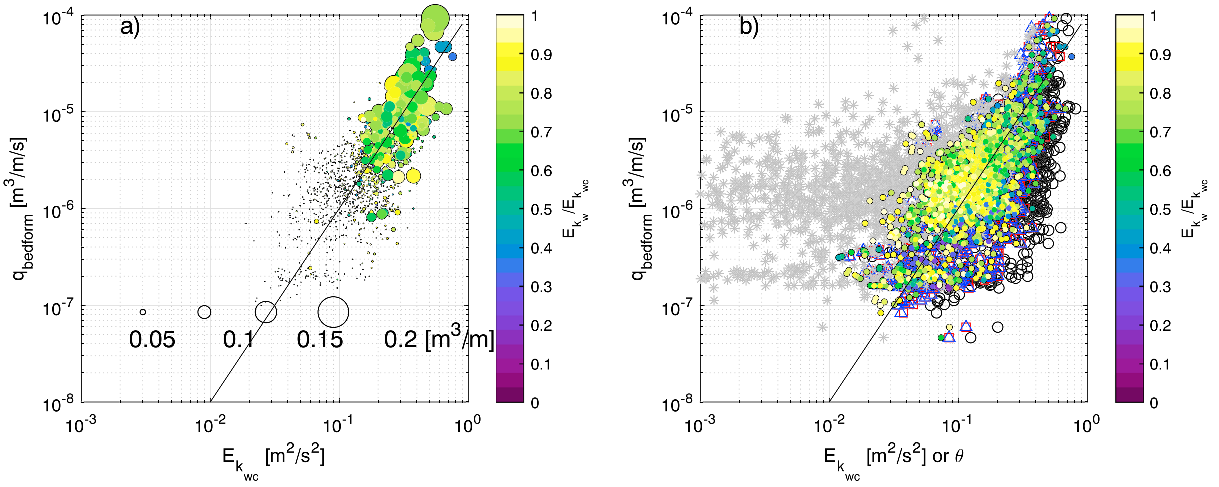

Figure 8. Observed bedform sediment transport flux, q_{bedform}, plotted against total kinetic energy, $E_{k_{wc}}$, (panel a), and plotted against the total kinetic energy and the Shields parameter (panel b), on log-scale. $E_{k_{wc}}$ data are colored by the fraction of energy due to waves, to show flow dominance. Marker size in panel a is scaled with bedform volume, Λ_b, as shown in the bottom of the panel. Additionally, in panel (b), filled circles are again the kinetic energy shaded by fraction of energy due to waves ($r^2 = 0.63$), the black ○ indicate the Shields parameter from N92LA98 ($r^2 = 0.51$), the red □ indicate the Shields parameter from M94 ($r^2 = 0.58$), the blue △ indicate the Shields parameter from SG00 ($r^2 = 0.56$), and the gray ★ indicate the Shields parameter from SC05 ($r^2 = 0.49$). The solid black line is a fit line described as $q_{\text{bedform}} = 1 \times 10^{-4} E_{k_{wc}}^2$.

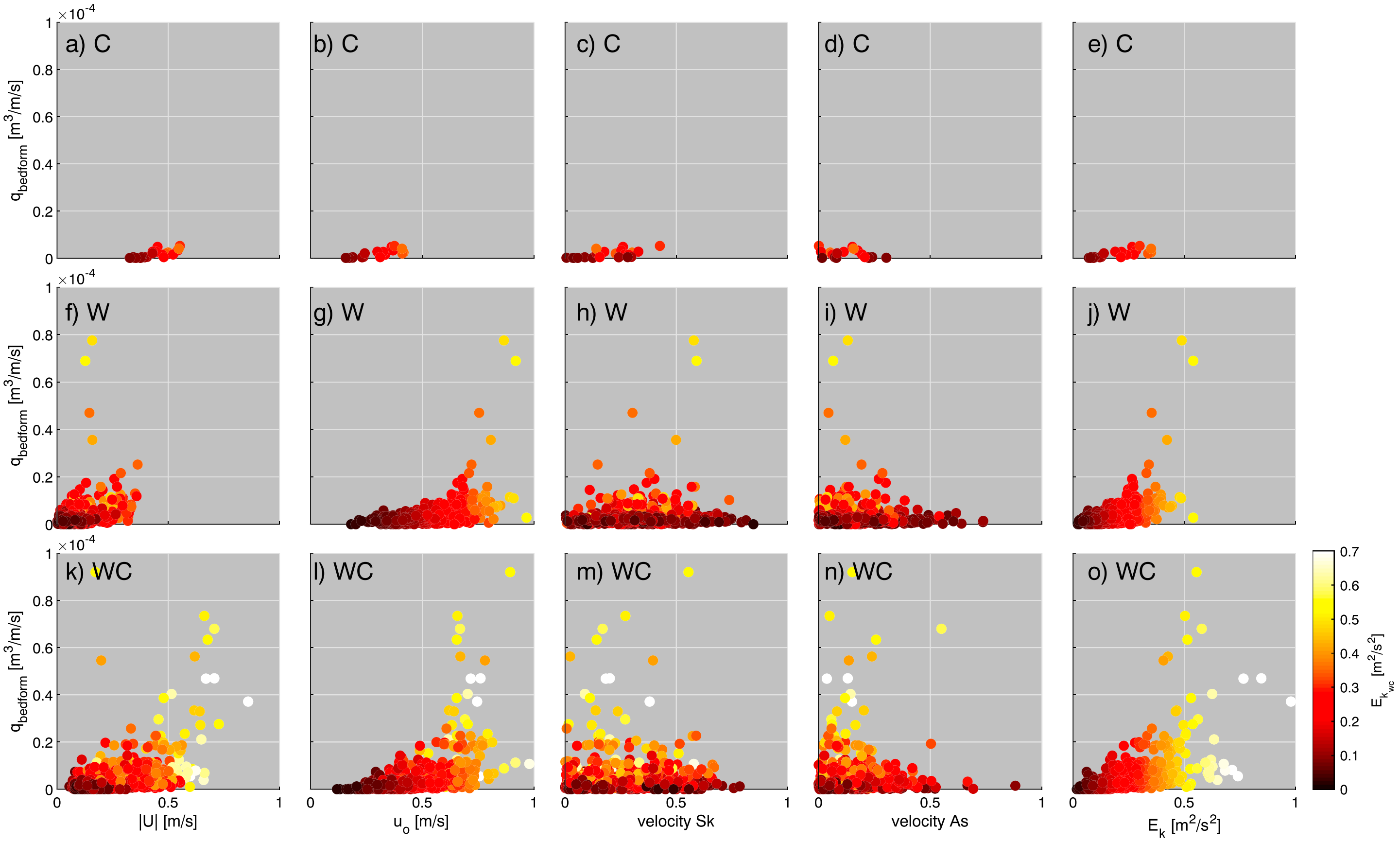

Figure 9. Indicators of the flow field, U, u_o, velocity Sk, velocity As, E_k plotted against the bedload sediment flux due to bedform migration, q_{bedform}, and colored by the total kinetic energy in the combined wave-currents, $E_{k_{\mathrm{wc}}}$. Panels (a)–(e) show current-dominant flows (fraction of energy due to waves <0.25); panels (f)–(j) show wave-dominant flows (fraction of energy due to waves >0.75); panels (k)–(o) show combined wave-current flows (fraction of energy due to waves is between 0.25 and 0.75).

following a power law relationship with a correlation of $r^2 = 0.63$ (Figure 8a). Additionally, as total kinetic energy increases, so did the bedform volume, (volume is represented with marker size in Figure 8a) and bedforms transporting the most sediment are influenced (at least somewhat) by currents (occurring when there was a low fraction of kinetic energy due to waves; green to blue colors on Figure 8a).

Observations show that the flow total kinetic energy was more highly correlated to the bedload sediment flux without any tuning when compared with friction factor based methods used to estimate the Shields parameter, θ ($r^2 = 0.49$–0.58). Both flow total kinetic energy and bed shear stress follow a u^2 relationship; bedload transport formulations based upon either the total kinetic energy or the Shields parameter raise the metric to a higher power, usually to the $\frac{3}{2}$ power in both cases. Figure 8b plots both $E_{k_{\mathrm{wc}}}$ and θ against the observed bedload transport rate. Estimates of θ show more scatter between methods in comparison with the flow kinetic energy when plotted against the bedload sediment transport rate (Figure 8b). Depending upon the method used to estimate the nondimensional shears stress, approximations of the bedload sediment transport rate vary significantly. The combined wave current M94 method and the SG00 methods to estimate the nondimensional bed shear stress show the best comparison to the bedload sediment transport rate (Figure 8b). Further discussion of estimates of sediment transport when the nondimensional shear stress models are used in the explicit sediment transport models follows in the next Section.

Quantitatively, bedform migration magnitude increased with increasing flow energy regardless of whether the flow was wave-dominant, current-dominant, or combined wave-current (panel b in Figures 2–5; Figure 6). Analysis shows that the maximum migration velocity and in turn the largest sediment transport rates were concomitant with a peak in the total kinetic energy and/or the period when the bedform orientation was aligned with the bedform migration direction (Figures 2–5). The total energy contained in the flow

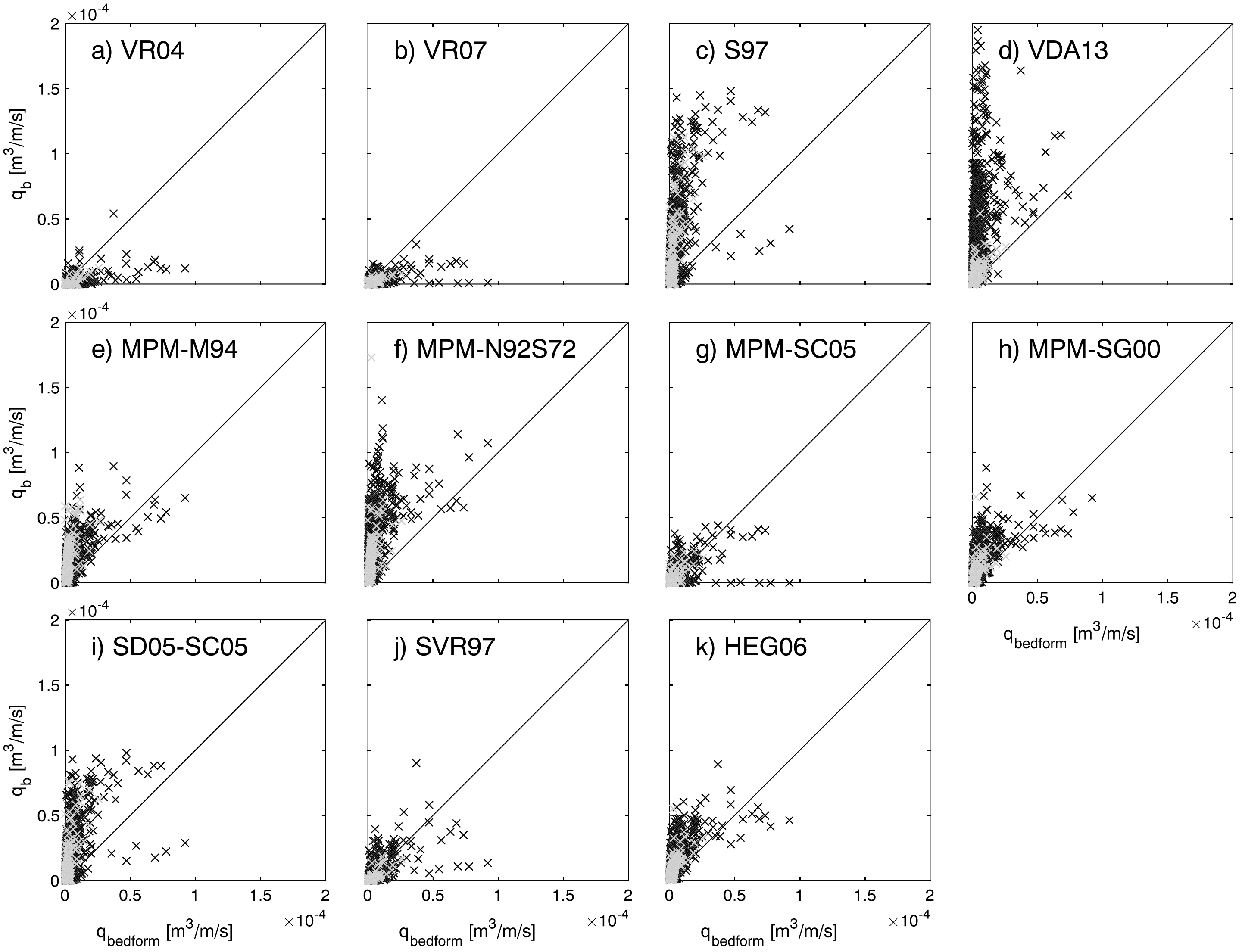

Figure 10. Data-model comparisons of bedload sediment flux from bedform migration (q_{bedform}) to bedload transport models (q_b). Transport measurements were instantaneous. In black × are data from S1 and in gray ∘ are data from S2. The solid black line is a 1:1 ratio. The following are panels paired with the transport model reference: (a) van Rijn et al. (2004) transport model, (b) van Rijn (2007) transport model, (c) Soulsby (1997) transport model, (d) van der A et al. (2013) semiunsteady transport model, (e) Meyer-Peter and Muller (1948) transport model with Madsen (1994) bed stress model, (f) Meyer-Peter and Muller (1948) transport model with Nielsen (1992) wave bed stress model and Sternberg (1972) current bed stress model, (g) Meyer-Peter and Muller (1948) transport model with Soulsby and Clarke (2005) bed stress model, (h) Meyer-Peter and Muller (1948) transport model with Styles and Glenn (2000) bed stress model, (i) Soulsby and Damgaard (2005) transport model with Soulsby and Clarke (2005) bed stress model, (j) Soulsby-van Rijn transport model published in Soulsby (1997), and (k) Hsu et al. (2006) energetics transport model. For reference, every step increase of 0.1 $\times 10^{-4}$ $m^3/m/s$ is equivalent to an increase of 10 $cm^3/m/s$.

was proportional to the overall contribution of bedform migration to bedload sediment flux (Figures 8 and 9).

4.2. Bedform Sediment Flux Compared With Existing Bedload Transport Models

Bedload transport models rely on either a bed stress approach or an energetics approach. Eleven different bedload transport models—all formulated to work in combined flows—are compared to observations of bedload transport due to bedform migration for both site S1 and site S2 (Figure 10 and Table 1). Models presented in panels (a)–(d) have an imbedded friction factor and drag coefficient to estimate stress within the bedload transport formulation, models presented in panels (e)–(i) are transport models that depend on an outside bed shear stress approximation measurement or model, and the models presented in panels (j)–(k) use an energetics approach. The model abbreviations used in this section and in Figure 10 are given in Table 1.

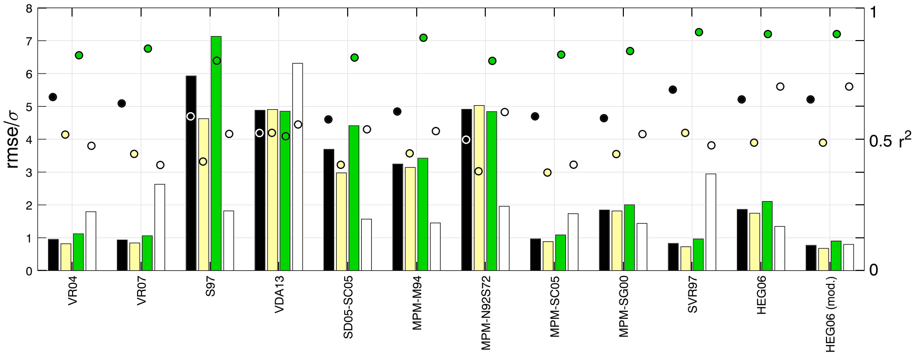

Figure 11. Data-model comparison statistics of rmse/σ (bars) and r^2 (×) for the bedload sediment transport models shown in Figure 10. The black bars show linear statistics for the entire time series (*all data*) collected at S1 and S2, the light bars yellow bars show linear statistics for *wave* dominant flows only ($E_{k_w}/E_{k_{wc}} > 0.75$), the green bars show linear statistics for *combined* flow data only ($E_{k_w}/E_{k_{wc}}$ is between 0.25 and 0.75), and the white bars show logarithmic statistics for the entire time series (*all data*) collected at S1 and S2. Current-dominant flow statistics are not shown because of low data availability.

Some models underpredicted bedload transport (VR04 and VR07), many overpredicted transport (S97, SD05-SC05, MPM-M94, MPM-N92S72, MPM-SG00, HEG06, and VDA13), and two models are qualitatively consistent (SVR97 and MPM-SC05). Figure 11 shows calculated rmse/σ and r^2 for data from both the S1 and S2 sites for the whole data set (*all data*) in both linear and log-scale, for *wave*-dominant flows only in linear scale ($E_{k_w}/E_{k_{wc}} > 0.75$), and for *combined* flow data only in linear-scale ($0.25 < E_{k_w}/E_{k_{wc}} < 0.75$). Data were portioned to demonstrate which models perform best overall and which perform best in specifically combined flow conditions.

First, we compared the intramodel portioned cases, *all data*, *combined*, and *wave*, to one and other. Interestingly, the *combined* flow case had the highest rmse/σr^2 for each combined flow sediment transport model when compared with the *wave* and *all data* cases, showing that even though the model fit the trend of the observations well, it also had the largest deviations of the three cases. The *wave* case had the lowest rmse/σ of all cases and also the lowest r^2, showing the opposite: the model fit the trend of the observations poorly, yet had the smallest deviations. It is worth while to note that the least squares and rmse/σ calculations in linear scale are biased toward the smaller wavelength ripples because they occurred more frequently at the site, even though they were shown to not be as important to bedload sediment flux as larger wavelength bedforms. For that reason, we also calculated the rmse/σ and r^2 in log-scale; the log-scale calculations show a better representation of the models that are able to capture both small and large instances of transport. For most models on the log-scale, the r^2 decreases, but for the models that are biased toward predicting lower transport periods well, the rmse/σ increases (as is the case with VR04 and VR07).

Most of the models evaluated tend to over predict bedload transport when compared to bedform transport rates (Figure 10). The SVR97 model was the only model that had an *rmse*/σ of 1 or less in all three cases on linear scale (*all data*, *combined*, and *wave*), but on log-scale, the rmse/σ increases and r^2 decreases for SVR97. Four models had a linear r^2 of 0.60 or greater within the *all data* condition (VR04, VR07, SVR97, and HEG06). Within the *combined* subset most models had a linear r^2 of approximately 0.7, but for the *wave* subset the linear r^2 dropped to approximately 0.5. Overall, on linear-scale SVR97 (Figure 10j) performed the best, followed by the MPM-SC05 (Figure 10g), but on log-scale both were shown to predict larger periods of transport less well. The VR04 and VR07 models performed well during lower-energy conditions, but the scatter (Figures 10a and 10b) shows that both models largely under predict during periods with the largest transport rates and that is confirmed by the logarithmic *rmse*/σ increase. The under prediction of large flux is a problem for implementation in coastal change models since these large sediment flux events have been shown to highly influence morphologic evolution (de Schipper et al., 2016). VDA13 is a semiunsteady model that includes the effects of wave skewness on transport, but it has not yet been tested in combined flows over ripples, and in these conditions it over predicts transport.

Both SVR97 and HEG06 were formulated as an energetics type models. Flow total kinetic energy has a high correlation ($r^2 = 0.63$) with bedform sediment flux and provides a foundation for relating flow field energy

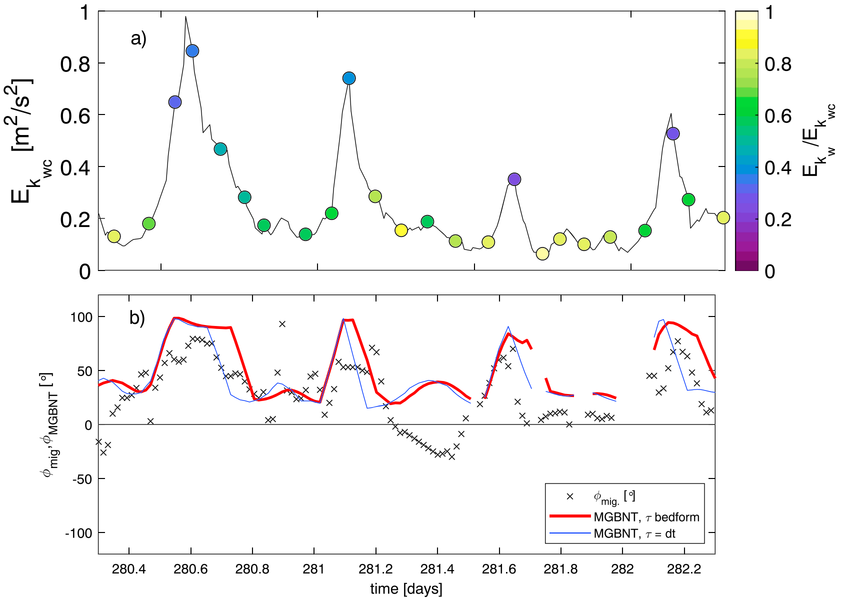

Figure 12. Truncated time series showing bedform migration direction, $\phi_{\mathrm{mig.}}$, and modeled direction, ϕ_{MGBNT}. Panel (a) shows the total kinetic energy, $E_{k_{wc}}$ colored by fraction of energy due to waves, and panel (b) shows bedform migration direction, $\phi_{\mathrm{mig.}}$, observed (×) and modeled, ϕ_{MGBNT} (red and blue lines). MGBNT was calculated using an adjustment time, τ, related to the bedform growth lag time (red, $r^2 = 0.28$, rmse = 32°), and the sampling frequency (blue, dt = 20 min, $r^2 = 0.24$, rmse = 40°). MGBNT = maximum gross bedform normal transport.

to the bedload sediment transport rate (Figures 8 and 9). All estimates of the Shields parameter (without high-resolution boundary layer measurements) must incorporate a friction factor; however, the flow field total kinetic energy has a high skill with bedload sediment flux without friction factors or tuning. SVR97 has a drag coefficient that considers both logarithmic boundary layer scaling (for currents) and turbulent kinetic energy produced by the combined wave current boundary layer over a rippled bed (Soulsby, 1997), building blocks that fully describe conditions of our observations. The model also predicted periods with large transport rates to higher skill than the other models (Figure 10). The Bagnold (1966), Bowen (1980), and Bailard and Inman (1981) family of energetics models (here HEG06) have a foundation in flow field total kinetic energy but have a u^3 relationship that accounts for wave orbital motion as well as mean flow and wave-induced currents for bedload transport, an efficiency of transport parameter (percent of energy in the flow field that is transferred to bed mobility), and a friction coefficient. HEG06 has one of the lowest rmse/σ and highest r^2 values of all the tested models in linear scale, and its overall rmse/σ and r^2 improve on log-scale, showing that it is well suited to estimate bedload transport in mild as well as energetic flows.

The energetics model in Hsu et al. (2006, HEG06) use wave and current friction coefficients that were “tuned” for sandbar mobility, where bedload transport is generally sheet flow driven. The friction coefficient may be different when applied to bedform migration, either because the flow obstacle geometry is smaller or because the dominant process of bedload transport are different (predominantly sheet flow over the sandbar whereas during bedform migration mechanisms include rolling, jumping, and marching). Since sand ripples/bedforms are smaller than sandbars, and/or the type of bedload transport occurring during bedform migration requires less energy, it is logical for the friction coefficient to decrease to fit the bedload transport due to bedform migration condition. The high skill between the flow field kinetic energy and the bedload sediment flux justifies tuning the current and wave friction coefficients to fit the rippled bed flow environment. If the friction coefficients are decreased by 60% and the transport efficiency remains unchanged in Hsu et al. (2006), the model rmse/σ and r^2 becomes the best correlated to the observations compared with the *all data*, *combined*, and *wave* cases (see Figure 11 HEG06, mod.).

4.3. Bedform Migration Direction and Bedload Sediment Transport Direction

Gallagher et al. (1998) and Lacy et al. (2007) show that the bedform migration direction has some relationship with the prevailing flow field using MGBNT from (6). The bedform migration direction, $\phi_{\mathrm{mig.}}$, and the MGBNT direction ϕ_{MGBNT} are shown in a truncated time series in Figure 12b, with the total energy in the flow field plotted for reference in Figure 12a. As described in Gallagher et al. (1998) for the MGBNT to accurately describe the bedform orientation, the flow vectors (containing both waves and currents) must be summed over the timescale of bedform development, implying a time dependence between flow direction and bedform migration direction. In Wengrove et al. (2018), an adjustment time, τ, is suggested as the integration timescale in order to predict bedform growth. The timescale may also be relevant in predicting bedform migration direction. The MGBNT including the variable adjustment timescale from Wengrove et al. (2018) (red), as well as with a constant adjustment timescale equal to the sampling rate, dt, (blue), is compared with the observed bedform migration direction in Figure 12b. The variable adjustment timescale did not significantly increase MGBNT model skill. However, the variable adjustment timescale did influence the duration that a migration direction peak persisted and the bedform wavelength(Figure 12b; Wengrove et al., 2018). Bedform migration direction was compared to MBGNT direction prediction using circular statistics, ϕ_{MGBNT}, MGBNT using an adjustment time related to bedform growth had a $r^2 = 0.28$, rmse/$\sigma =$ 32°; MGBNT using an adjustment time of the dt had a $r^2 = 0.24$, rmse/$\sigma = 40°$ in (Figure 7c). MGBNT did estimate transport direction better than the current or wave directions alone. However, use of the variable adjustment time did not improve prediction. Qualitatively, MGBNT predictions vary with $\phi_{\mathrm{mig.}}$, but temporal lags between predictions and measurements reduce correlations. In Lacy et al. (2007) the MGBNT method fits the measured transport direction at times and also shows significant deviations for approximately 20% of the data shown (see Lacy et al., 2007, Figure 17d).

Overall, the bedform migration direction was difficult to predict in these data. The difficulty of prediction may be due to the bedform dynamics not considered and the large variability in the flow directions and strengths. The MGBNT method appears to be the best model to describe dynamic bedforms, but the bedform growth timescale may not be characteristic of the change in migration direction. The bedform migration direction leads the bedform orientation direction as well as the bedform growth (Figures 2–5).

The bedform migration direction is not necessarily the same as the bedload transport direction, as seen in the difference between the observed bedform orientation and observed bedload sediment transport directions (Figures 2–5). The contribution of both current direction as well as wave nonlineartity is important to estimating the sediment transport direction in combined flows. Of the eleven bedload sediment transport models evaluated to approximate bedload sediment transport magnitudes in combined flows here, only two of the models explicitly account for currents as well as wave nonlinearties in estimating transport (Hsu et al., 2006; van der A et al., 2013). Other models tested may account for wave nonlinearities through wave driven currents (e.g., Soulsby and van Rijn ; Soulsby, 1997); however, model skill with respect to bedload transport direction was not evaluated further in this effort.

5. Conclusion

Our effort contributes unique field observations made in the surf zone of bedform response to wave dominant, current dominant, in addition to characterizing the bedload sediment transport response to combined wave-current flow conditions. Increased sediment flux was driven predominantly by increased total kinetic energy in the flow field. Individually, the wave-dominant, current-dominant, and combined wave-current conditions had characteristic differences in bedform shape, migration direction with respect to the overlying flow directions, and mechanisms driving sediment flux. During wave dominant flow conditions, the bedform wavelength could vary dependent on the orbital excursion of the waves (in this data set Λ ~0.20–1.5 m). When the bedforms began to migrate most rapidly ($V_{\mathrm{mig.}} > 1$ cm/min), the waves were skewed and the sediment transport direction and the bedform orientation were aligned. During current-dominant flow conditions, bedforms were long in wavelength (Λ ~1 m), but there was not enough total flow field energy to cause these bedforms to migrate, so the overall sediment flux due to currents alone was low. Additionally, the sediment transport direction visibly led the bedform orientation direction. During combined flow conditions the bedforms could get very large in wavelength (Λ ~1–2.5 m) and volume. During the highest energy conditions characteristic of strong current velocities and almost equally as strong wave orbital velocities, the combined flow bedforms evolved into lunate megaripples with their migration direction somewhat aligned with the predominant flood tidal current direction. Additionally, combined flow bedforms migrated the most when the sediment transport direction and the bedform orientation were aligned.

Observations show that combined wave-current bedforms had higher sediment flux rates than current-dominant and wave-dominant bedforms. The sediment flux magnitude associated with bedform mobility within combined wave-current flows was on average 24% (15%) greater in mean (median) than wave dominant flows and 82% (91%) greater in mean (median) than current-dominant flows. A result suggesting that although waves are still dominant in the nearshore region, combined wave-current flows increase sediment transport rates significantly and therefore are important to consider when predicting coastal morphodynamics.

Eleven existing bedload transport models used in large-scale coastal change models were assessed. Each model is specifically formulated to estimate transport and bed stress in combined wave-current flows by either taking a stress ($q_b = f(\tau_b)$) or an energetics ($q_b = f(u^n)$) based approach. Our observations show that the bedload sediment flux was directly proportional and strongly correlated to the total kinetic energy in the flow field. Suggesting that a transport model with foundation in hydrodynamic kinetic energy may be the most characteristic of the system considering our present measurement and modeling capabilities. The energetics based approaches predicted bedload transport in both calm and energetic conditions with low normalized $rmse/\sigma$ and high r^2 on linear and log-scales. The Soulsby/van Rijn (Soulsby, 1997) bedload transport model was formulated with the turbulent kinetic energy in combined flows over ripples, which was characteristic of the observed conditions. In the Bagnold (1966), Bowen (1980), and Bailard and Inman (1981) line of energetics models, the Hsu et al. (2006) formulation captures wave orbital motion as well as mean and wave-induced currents. In Hsu et al. (2006), the wave and current friction coefficients were based on bedload transport associated with sandbar mobility. If these friction coefficients are decreased to account for differences in length scales (sandbar vs. ripple geometry) and timescales of transport mode (sheet flow for sandbar mobility vs. bedform migration for ripples), then the Hsu et al. (2006) energetics approach had the lowest linear and log-scale rmse/σ and the highest r^2 of all the assessed transport models. The caveat with most bedload sediment transport models is that many do not explicitly include wave nonlinearity in their transport approximations and therefore do not explicilty account for wave-induced bedload transport direction through wave velocity skewness and asymmetry. The series of energetics models do include wave asymmetry (Bailard & Inman, 1981; Hsu et al., 2006). In field and laboratory campaigns and within numerical data sets, an energetics approach to estimate sediment transport may yield higher skill results and lead to less propagation of error in prediction of bedload sediment transport when compared with excess shear based approaches; especially when measurements or model results are too coarse to accurately estimate or measure the bed shear stress.

Acknowledgments
We would like to acknowledge the team of graduate students, technicians, and faculty members from multiple countries and institutions who contributed to MEGAPEX. MEGAPEX was funded through NWO grant 12686, Nature Coast, and ERC Advance grant 91206, and NEMO. The UNH contribution to MegaPEX was funded by the PADI Foundation. M. E. W. was supported by the U.S. Department of Defense NDSEG fellowship. D. L. F. was funded by NSF grant 1135026. T. C. L. was funded under ONR contract N00014-14-1-0557. M. d. S. was supported by NWO grant 15058, Feeding Starved Coasts by Morphological Diffusivity. J. C. was supported under base funding to the U.S. Naval Research Laboratory from the Office of Naval Research. Data from MegaPEX can be found at data.4tu.nl/repository/collection: zandmotor website.

References

Aagaard, T., Greenwood, B., & Nielsen, J. (2001). Bed level changes and megaripple migration on a barred beach. *Journal of Coastal Research*, 110–116.

Amos, C., Bowen, A., Huntley, D., Judge, J., & Li, M. (1999). Ripple migration and sand transport under quasi-orthogonal combined flows on the scotian shelf. *Journal of Coastal Research*, *15*, 1–14.

Bagnold, R. (1966). An approach to the sediment transport problem from general physics, Prof. Paper 422-1, U.S.G.S.

Bailard, J., & Inman, D. (1981). An energetics bedload transport model for a plane sloping beach: Local transport. *Journal of Geophysical Research*, *86*, 2035–2043.

Bowen, A. J. (1980). Simple models of nearshore sedimentation; beach profiles and longshore bars. The Coastline of Canada.

Catano-Lopera, Y. A., & Garcia, M. H. (2006). Geometry and migration characteristics of bedforms under waves and currents part 2: Ripples superimposed on sandwaves. *Coastal Engineering*, *53*, 781–792.

Davies, A. G., & Villaret, C. (1999). Eulerian drift induced by progressive waves above rippled and very rough beds. *Journal of Geophysical Research*, *104*(C1), 1465–1488.

de Schipper, M. A., de Vries, S., Ruessink, G., de Zeeuw, R. C., Rutten, J., van Gelder-Mass, C., & Stive, M. J. F. (2016). Initial spreading of a mega feeder nourishment: Observations of the sand engine pilot project. *Coastal Engineering*, *111*, 23–38.

Foster, D. L., Bowen, A. J., Holman, R. A., & Natoo, P. (2006). Field evidence of pressure gradient induced incipient motion. *Journal of Geophysical Research*, *111*, C05004. https://doi.org/10.1029/2004JC002,863

Fredsøe, J., Andersen, K. H., & Mutlu Sumer, B. (1999). Wave plus current over a ripple-covered bed. *Coastal Engineering*, *38*, 177–221.

Fredsøe, J., & Deigaard, R. (1992). *Mechanics of coastal sediment transport*. Singapore: World Scientific.

Gallagher, E. L., Elgar, S., & Thornton, E. B. (1998). Megaripple migration in a natural surf zone. *Letters to Nature*, *394*, 165–168.

Grant, W. D., & Madsen, O. S. (1979). Combined wave and current interaction with a rough bottom. *Journal of Geophysical Research*, *84*(C4), 1797–1808.

Hay, A. E., & Mudge, T. (2005). Principal bed states during sandyduck97: Occurrence, spectral anisotropy, and the bed state storm cycle. *Journal of Geophysical Research*, *110*, C03013. https://doi.org/10.1029/2004JC002451

Hsu, T.-J., Elgar, S., & Guza, R. T. (2006). Wave-induced sediment transport and onshore sandbar migration. *Coastal Engineering*, *53*, 817–824.

Lacy, J. R., Rubin, D. M., Ikeda, H., Mokudai, K., & Hanes, D. M. (2007). Bed forms created by simulated waves and currents in a large flume. *Journal of Geophysical Research*, *112*, C10018. https://doi.org/10.1029/2006JC003942

Lesser, G. R., Roelvink, J. A., van Kester, T. M., & Stelling, G. S. (2004). Development and validation of a three-dimensional morphological model. *Coastal Engineering*, *51*, 883–915.

Madsen, O. (1994). Spectral wave-current bottom boundary layer flows. In *Coastal Engineering '94, Proceedings of the 24th International Conference*, Coastal Engineering Research Council, American Society of Civil Engineers, Kobe, Japan, pp. 384–398.

Mathisen, P. P., & Madsen, O. S. (1996). Waves and currents over a fixed rippled bed 1. Bottom roughness experienced by waves in the presence and absence of currents. *Journal of Geophysical Research*, *101*, 16,533–16,542.

Meyer-Peter, E., & Muller, R. (1948). Formulas for bed-load transport. In *Report on the Second Meeting of the International Association for Hydraulic Structures Research*, Stockholm, pp. 39–64.

Ngusaru, A. S., & Hay, A. E. (2004). Cross-shore migration of lunate megaripples during duck94. *Journal of Geophysical Research*, *109*, C02006. https://doi.org/10.1029/2002JC001532

Nielsen, P. (1992). *Coastal bottom boundary layers and sediment transport*. Singapore: World Scientific.

Nielsen, P., & Callaghan, D. (2003). Shear stress and sediment transport calculations for sheet flow under waves. *Coastal Engineering*, *47*(3), 347–354.

Passchier, S., & Kleinhans, M. G. (2005). Observations of sand waves, megaripples, and hummocks in the dutch coastal area and their relation to currents and combined flow conditions. *Journal of Geophysical Research*, *110*, F04S15. https://doi.org/10.1029/2004JF000215

Perillo, M. M., Best, J. L., Yokokawa, M., Sekiguchi, T., Takagawa, T., & Garcia, M. H. (2014). A unified model for bedform development and equilibrium under unidirectional, oscillatory and combined flows. *Sedimentology*, *61*, 2063–2085. https://doi.org/10.1111/sed.12129

Perkovic, D., Lippmann, T., & Frasier, S. (2009). Longshore surface currents measured by doppler radar and video piv techniques. *IEEE Transactions on Geoscience and Remote Sensing*, *47*(8), 2787–2800. https://doi.org/10.1109/TGRS.2009.2016556

Rodriguez-Abudo, S. A., & Foster, D. L. (2014). Unsteady stress partitioning and momentum transfer in the wave bottom boundary layer over movable rippled beds. *Journal Geophysical Research: Oceans*, *119*, 8530–8551. https://doi.org/10.1002/2014JC010240

Roelvink, D. J. A., van Dongeren, A., McCall, R. T., & Hoonhout, B. (2015). Xbeach technical reference: Kingsway release, User manual. Daltares.

Shields, A. (1936). Anwendung der anhlichkeitsmechanik und turbulenzforschung auf die geschiebebewegung, Mitt. *Preuss Versuchsanstalt fur Wassebaur und Schiffbau*, *26*.

Sleath, J. F. A. (1999). Conditions for plug formation in oscillatory flow. *Continental Shelf Research*, *19*, 1643–1664.

Smyth, C., & Li, M. (2005). Wave-current bedform scales, orientation, and migration on sable island bank. *Journal of Geophysical Research*, *110*, C02023. https://doi.org/10.1029/2004JC002569

Soulsby, R. L. (1997). *Dynamics of marine sands* (1st ed.).: Thomas Telford Services, Ltd.

Soulsby, R., & Clarke, S. (2005). Bed shear-stresses under combined waves and currents on smooth and rough beds (*Report TR 137*). HR Wallingford.

Soulsby, R. L., & Damgaard, J. S. (2005). Bedload sediment transport in coastal waters. *Coastal Engineering*, *52*, 673–689.

Soulsby, R. L., Whitehouse, R. J. S., & Marten, K. V. (2012). Prediction of time-evolving sand ripples in shelf seas. *Continental Shelf Research*, *38*, 47–62.

Sternberg, R. (1972). Predicting initial motion and bedload transport of sediment particles in the shallow marine environment. *Shelf Sediment Transport: Process and Pattern*.

Styles, R., & Glenn, S. M. (2000). Modeling stratified wave and current bottom boundary layers on the continental shelf. *Journal of Geophysical Research*, *105*(C10), 24,119–24,139.

Thornton, E. B., Swayne, J. L., & Dingler, J. R. (1998). Small-scale morphology across the surf zone. *Marine Geology*, *145*, 173–196.

Traykovski, P., Hay, A. E., Irish, J. D., & Lynch, J. F. (1999). Geometry, migration, and evolution of wave orbital ripples at leo-15. *Journal of Geophysical Research*, *104*(C1), 1505–1524.

van Rijn, L. (1993). *Principles of sediment transport in rivers estuaries and coastal seas*. The Netherlands: Aqua Publications.

van Rijn, L. C. (2007). Unified view of sediment transport by currents and waves. I: Initiation of motion, bed roughness, and bed-load transport. *Journal of Hydraulic Engineering*, *6*, 649–667.

van Rijn, L. C., Walstra, D. J. R., & Ormondt, M. (2004). Description of transpor2004 and implementation in delft3d-online: Final report (*Tech. Rep.*) Deltares.

van der A, D. A., Ribberink, J. S., van der Werf, J. J., O'Donoghue, T., Buisrogge, R. H., & Kranenburg, W. M. (2013). Practical sand transport formula for non-breaking waves and currents. *Coastal Engineering*, *76*, 26–42.

Warner, J., Sherwood, C., Signell, R., Harris, C., & Arango, H. (2008). Development of a three-dimensional, regional, coupled wave, current, and sediment-transport model. *Computers & Geosciences*, *34*(10), 1284–1306.

Wengrove, M. E., Foster, D. L., de Schipper, M. A., & Lippmann, T. C. (2017). Wave and current ripple formation and migration during storms. *Proceedings of Coastal Dynamics*, *129*, 955-965.

Wengrove, M. E., Foster, D. L., Lippmann, T. C., de Schipper, M. A., & Calantoni, J. (2018). Observations of time dependent bedform transformation in combined wave-current flows. *Journal of Geophysical Research: Oceans*, *123*, 7581–7598. https://doi.org/https://doi.org/10.1029/2018JC014357